

The electron temperatures of SDSS high-metallicity giant extragalactic H II regions

L.S. Pilyugin¹, J.M. Vílchez², B. Cedrés² and T.X. Thuan³

¹ *Main Astronomical Observatory of National Academy of Sciences of Ukraine, 27 Zabolotnogo str., 03680 Kiev, Ukraine*

² *Instituto de Astrofísica de Andalucía, CSIC, Apdo, 3004, 18080 Granada, Spain*

³ *Astronomy Department, University of Virginia, P.O.Box 400325, Charlottesville, VA 22904-4325*

Accepted 2009 Month 00. Received 2009 December 2; in original form 2009 October 26

ABSTRACT

Spectra of high-metallicity ($12+\log(\text{O}/\text{H}) \gtrsim 8.2$) H II regions where oxygen auroral lines are measurable in both the O^+ and O^{++} zones, have been extracted from the Data Release 6 of the Sloan Digital Sky Survey (SDSS). Our final sample consists of 181 SDSS spectra of H II regions in galaxies in the redshift range from ~ 0.025 to ~ 0.17 . The $t_{2,\text{O}}-t_{3,\text{O}}$ diagram is examined. In the SDSS H II regions, the electron temperature $t_{2,\text{O}}$ is found to have a large scatter at a given value of the electron temperature $t_{3,\text{O}}$. The majority of the SDSS H II regions lie below the $t_{2,\text{O}}-t_{3,\text{O}}$ relation derived for H II regions in nearby galaxies, i.e. the positions of the SDSS H II regions show a systematic shift towards lower $t_{2,\text{O}}$ temperatures or/and towards higher $t_{3,\text{O}}$ temperatures. The scatter and shift of the SDSS H II regions in the $t_{2,\text{O}}-t_{3,\text{O}}$ diagram can be understood if they are composite nebulae excited by two or more ionizing sources of different temperatures.

Key words:

galaxies: abundances – ISM: abundances – H II regions

1 INTRODUCTION

The determination of chemical abundances in cosmic objects started 150 years ago, when Gustav Kirchhoff and Robert Bunsen discovered the laws of spectroscopy and founded the theory of spectrum analysis. In particular, they discovered that each atom exhibits a specific pattern of spectral lines, and that, therefore, by observing an object’s spectrum, one can deduce, among other things, its composition and physical conditions. Kirchhoff applied spectral analysis techniques to study the chemical composition of the Sun. Many astronomers and physicists have made subsequent contributions to the theory of spectrum analysis. However, at the present time, the equations linking the abundance of a chemical element to the measured line fluxes are still not beyond dispute.

Accurate oxygen abundances in H II regions can be derived via the classic T_e method, often referred to as the direct method. First, the electron temperature t_3 within the $[\text{O III}]$ zone and the electron temperature t_2 within the $[\text{O II}]$ zone are determined. Then the abundance is derived using the equations linking the ionic abundances to the measured line intensities and electron temperature. The ratio of nebular to auroral oxygen line intensities $Q_{3,\text{O}} = [\text{O III}]\lambda 4959 + \lambda 5007 / [\text{O III}]\lambda 4363$ is used for the t_3 determination. The ratio of nebular to auroral oxygen line in-

tensities $Q_{2,\text{O}} = [\text{O II}]\lambda 3727 + \lambda 3729 / [\text{O II}]\lambda 7320 + \lambda 7330$ (or the ratio of nebular to auroral nitrogen line intensities $[\text{N II}]\lambda 6548 + \lambda 6584 / [\text{N II}]\lambda 5755$) is used for the t_2 determination. It is common practice to derive one value of the electron temperature t_3 or t_2 from the measured indicator $Q_{3,\text{O}}$ or $Q_{2,\text{N}}$ and to use the t_2-t_3 relation for the determination of the other electron temperature. Thus, in many cases, the abundances derived by the direct method are dependent on the adopted t_2-t_3 relation. Those direct abundances are at the base of some recent empirical calibrations (Pilyugin 2000, 2001, 2003; Pilyugin & Thuan 2005; Pettini & Pagel 2004). So the abundances derived through those empirical calibrations are also dependent on the adopted t_2-t_3 relation.

H II region models are widely used to establish the t_2-t_3 relation. It is commonly accepted that there is one-to-one correspondence between the t_2 and t_3 electron temperatures. Several versions of a one-dimensional t_2-t_3 relation have been proposed. A widely used version is that by Campbell, Terlevich & Melnick (1986) (see also Garnett (1992)) based on the H II region models of Stasińska (1982). Other relations have been proposed by Pagel et al. (1992); Izotov, Thuan & Lipovetsky (1997) (based on H II region model calculations by Stasińska (1990)), and Deharveng et al. (2000) (based on H II re-

gion model calculations by Stasińska & Schaerer (1997)). Oey & Shields (2000) have found that the relation of Campbell, Terlevich & Melnick (1986) is reasonable for $t_3 > 1.0$ (t_3 is in units of 10^4K), however at lower temperatures, the models are more consistent with an isothermal nebula. We have derived a t_2 - t_3 relation based on the idea that the T_e method equation for O^{++}/H^+ applied to the O^{++} zone and that for O^+/H^+ applied to the O^+ zone must result in the same value of the oxygen abundance (Pilyugin, Vílchez & Thuan 2006).

There have been several attempts to establish the t_2 - t_3 relation using direct measurements of both t_2 and t_3 in H II regions. Kennicutt, Bresolin & Garnett (2003) have used the measured $Q_{3,\text{O}}$ and $Q_{2,\text{O}}$ values to derive $t_{3,\text{O}}$ and $t_{2,\text{O}}$, respectively, for a number of H II regions in nearby galaxies. Comparing $t_{2,\text{O}}$ to $t_{3,\text{O}}$, they found the surprising result that the two temperatures are uncorrelated for most of the objects in their sample. They noted that, while the exact cause of the absence of correlation is not known, a possible explanation is the contribution of recombination processes to the population of the level giving rise to the $[\text{O II}]\lambda 7320 + \lambda 7330$ lines. Izotov et al. (2006) found a correlation between the $t_{2,\text{O}}$ and $t_{3,\text{O}}$ derived for a sample of low-metallicity SDSS H II regions. Their $t_{2,\text{O}}$ - $t_{3,\text{O}}$ relation follows that predicted by photoionization models, but the scatter of the data points is large. Izotov et al. (2006) attributed the large scatter to substantial flux errors of the weak $[\text{O II}]\lambda 7320 + \lambda 7330$ emission lines.

Another interpretation of the scatter in the t_2 - t_3 diagram has been proposed. Hägele et al. (2006, 2008) and Pilyugin (2007) have suggested that there is not a one-to-one correspondance between t_2 and t_3 , but that the t_2 - t_3 relation is dependent on some parameter such as electron density or excitation parameter. On the other hand, Pilyugin et al. (2009) have found that there is a one-to-one correspondance between t_2 and t_3 for H II regions in nearby galaxies with weak nebular R_3 lines ($\log R_3 \lesssim 0.5$, see the definition of R_3 below). However, H II regions with strong nebular R_3 lines ($\log R_3 \gtrsim 0.5$) do not follow this relation. As a result, the one-to-one correspondance between t_2 and t_3 disappears if a sample contains H II regions with both weak and strong R_3 lines.

We wish to study here the $t_{2,\text{O}}$ - $t_{3,\text{O}}$ relation, using a large sample of H II regions extracted from the Sloan Digital Sky Survey (SDSS). The paper is organised as follows. The SDSS H II region sample is described in Section 2. The $t_{2,\text{O}}$ - $t_{3,\text{O}}$ diagram is discussed in Section 3. The origin of the scatter in that diagram is examined in Section 4. Section 5 presents the conclusions.

Throughout the paper, we will be using the following notations for the line fluxes:

$$\begin{aligned} R &= [\text{O III}]\lambda 4363 = I_{[\text{O III}]\lambda 4363}/I_{\text{H}\beta}, \\ R_2 &= [\text{O II}]\lambda 3727 + \lambda 3729 = I_{[\text{O II}]\lambda 3727 + \lambda 3729}/I_{\text{H}\beta}, \\ R_3 &= [\text{O II}]\lambda 4959 + \lambda 5007 = I_{[\text{O II}]\lambda 4959 + \lambda 5007}/I_{\text{H}\beta}, \\ [\text{O II}]\lambda 7325 &= [\text{O II}]\lambda 7320 + \lambda 7330 = I_{[\text{O II}]\lambda 7320 + \lambda 7330}/I_{\text{H}\beta}, \end{aligned}$$

With these definitions, the excitation parameter P can be expressed as:

$$P = R_3/(R_2 + R_3),$$

and the temperature indicators $Q_{2,\text{O}}$ and $Q_{3,\text{O}}$ can be expressed as:

$$Q_{2,\text{O}} = R_2/[\text{O II}]\lambda 7325,$$

$$Q_{3,\text{O}} = R_3/R.$$

The electron temperatures will be given in units of 10^4K .

2 SAMPLE DESCRIPTION

2.1 Galaxy selection

We construct our sample by selecting from the Data Release 6 of the SDSS spectra of H II regions which satisfy the following criteria: 1) the two auroral lines $[\text{O III}]\lambda 4363$ and $[\text{O II}]\lambda 7320 + \lambda 7330$ are detected; 2) the spectra have smooth line profiles. Particular attention was paid to the weak $[\text{O III}]\lambda 4363$ and $[\text{O II}]\lambda 7320 + \lambda 7330$ auroral lines since the accuracy of the electron temperature determination depends mainly on the measurement uncertainties of those emission lines; 3) the emission lines do not have a broad component, thus excluding all AGNs.

Applying these criteria, we selected around 400 spectra out of the original 1 200 000 in the DR6. Although we visually inspected all spectra, we do not claim any completeness for our sample. The line intensities in the selected SDSS spectra of the H II regions have been measured in the way described in Pilyugin & Thuan (2007). In brief, it can be illustrated by the following example concerning the $\text{H}\alpha$ line. The continuum flux level in the wavelength range from $\lambda_a = 6500\text{\AA}$ to $\lambda_b = 6650\text{\AA}$ is approximated by the linear expression

$$f_c(\lambda) = c_0 + c_1\lambda. \quad (1)$$

The values of the coefficients in Eq.(1) are derived by an iteration procedure. In the first step, the $\text{H}\alpha$ line region, from 6540\AA to 6590\AA is excluded, and all other data points are used to derive a first set of coefficients, using the least-squares method. Then, the point with the largest deviation is rejected, and a new set of coefficients is derived. The iteration procedure is continued until the differences between two successive values of $f_c(\lambda_a)$ and $f_c(\lambda_b)$ are less than $0.01f_c(\lambda_a)$ and $0.01f_c(\lambda_b)$ respectively.

The profile of each line is approximated by a Gaussian of the form

$$f(\lambda) = F \frac{1}{\sqrt{2\pi}\sigma} e^{-(\lambda-\lambda_0)^2/2\sigma^2}, \quad (2)$$

where λ_0 is the central wavelength, σ is the width of the line, and F is the flux in the emission line. If there is absorption, then this line is fitted by two Gaussians simultaneously. In this case, the total flux at a fixed value of λ is given by the expression

$$f(\lambda) = f_{\text{H}\alpha,\text{em}}(\lambda) + f_{\text{H}\alpha,\text{abs}}(\lambda) + f_c(\lambda). \quad (3)$$

The values of $F(\text{H}\alpha,\text{em})$, $\lambda_0(\text{H}\alpha,\text{em})$, $\sigma(\text{H}\alpha,\text{em})$, $F(\text{H}\alpha,\text{abs})$, $\lambda_0(\text{H}\alpha,\text{abs})$, $\sigma(\text{H}\alpha,\text{abs})$, are derived by requiring the mean difference

$$\epsilon = \sqrt{\frac{1}{n} \sum_{k=1}^{k=n} (f(\lambda_k) - f^{\text{obs}}(\lambda_k))^2} \quad (4)$$

between the measured flux $f^{\text{obs}}(\lambda_k)$ and the flux $f(\lambda_k)$ given by Eq.(3) to be minimum in the range $\lambda_a - \lambda_b$. A similar procedure is adopted in the cases of overlapping lines (e.g. $[\text{O II}]\lambda 3727$ and $[\text{O II}]\lambda 3729$).

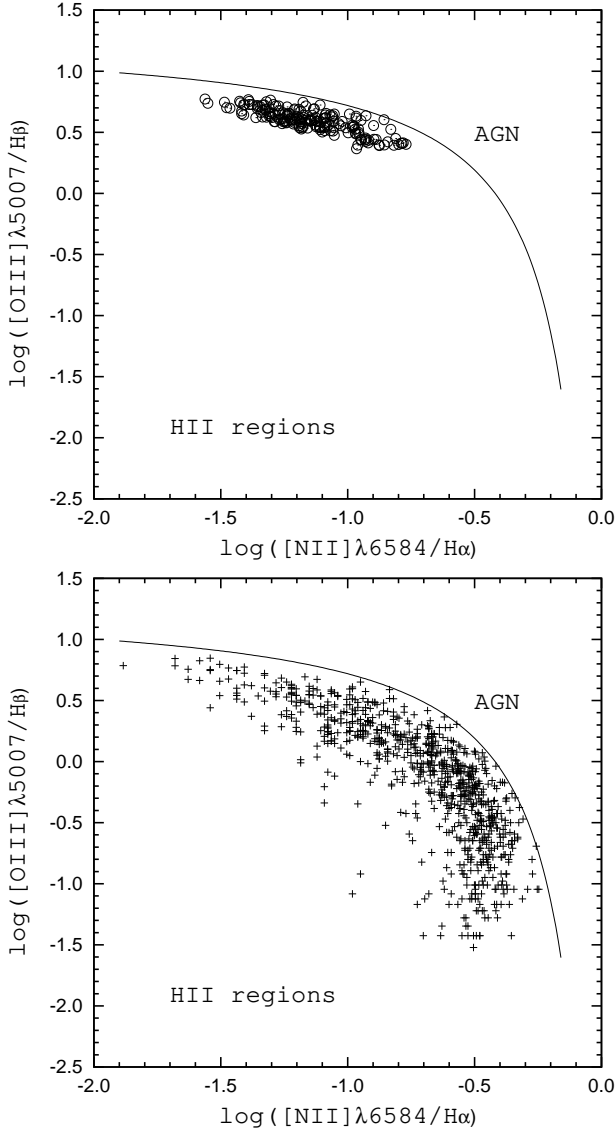


Figure 1. The $\text{N II} \lambda 6584 / \text{H} \alpha$ versus $[\text{O III}] \lambda 5007 / \text{H} \beta$ diagram for our sample of SDSS H II regions (*upper panel*) and for H II regions in nearby galaxies (a compilation of data from Pilyugin, Vílchez & Contini (2004)) (*lower panel*). The continuous line separates objects with a H II region-like spectrum from those containing an active galactic nucleus (Kauffmann et al. 2003).

In the majority of cases, the profile of each line is well fitted by a Gaussian since only spectra with smooth line profiles were selected. Thus, the uncertainties in the continuum level determination seem to make a dominant contribution to the uncertainties in the measurements of the weak auroral lines. The value of ϵ (Eq.(4)) is the mean uncertainty in the measurements of the flux in a single spectral interval. If we interpret this value as the uncertainty in the continuum level determination, the formal uncertainty in the measurements of the weak line intensity due to the uncertainty in the continuum level determination can be estimated as $\epsilon_F = n\epsilon$, where n is the number of points within the line profile.

Alternatively, the formal uncertainty in the weak line measurements defined in such a way can be interpreted as if

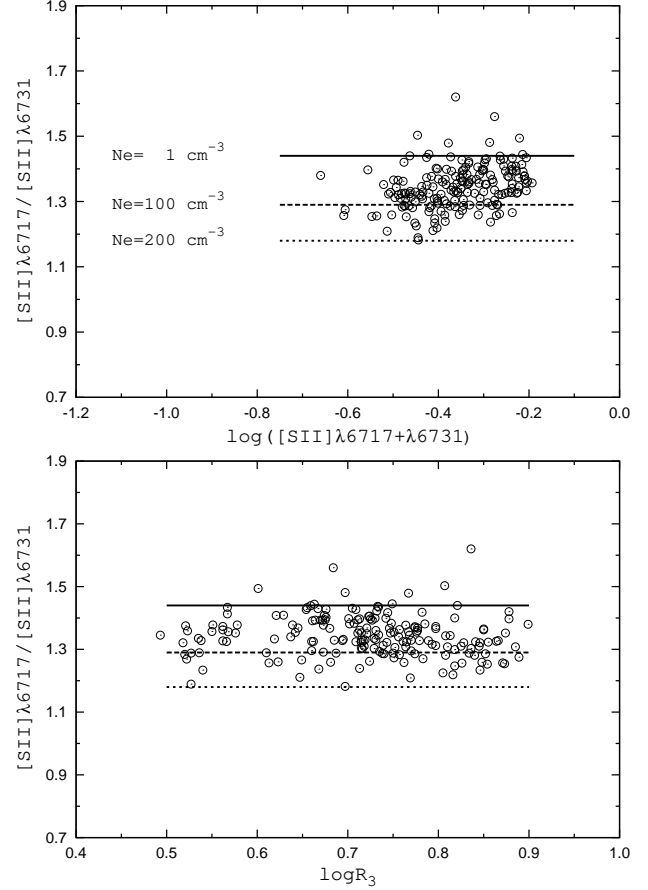


Figure 2. The density-sensitive $[\text{S II}] \lambda 6717 / [\text{S II}] \lambda 6731$ line ratio versus the $[\text{S II}] \lambda 6717 + \lambda 6731$ emission line flux (*top panel*) and versus the R_3 emission line flux (*bottom panel*). The open circles show the SDSS H II regions. The solid line shows the zero-density limit ($N_e = 1 \text{ cm}^{-3}$), the dashed line corresponds to the electron density $N_e = 100 \text{ cm}^{-3}$, and the dotted line corresponds to the electron density $N_e = 200 \text{ cm}^{-3}$.

the value of the continuum level is derived exactly and each point within the line profile involves an error equal to the mean uncertainty ϵ and all the errors have the same sign. One can expect that the formal uncertainty defined as $\epsilon_F = n\epsilon$ is close to the maximum possible error and that the real uncertainty in the line measurements is appreciably lower than this value. Consequently, the condition $\epsilon_F < 0.5$, when applied to both auroral lines $[\text{O III}] \lambda 4363$ and $[\text{O II}] \lambda 7325$, should select only objects with relatively precise line measurements, even though some objects with good measurements will be lost.

The measured emission fluxes are then corrected for interstellar reddening using the theoretical $\text{H} \alpha$ to $\text{H} \beta$ ratio and the analytical approximation to the Whitford interstellar reddening law from Izotov, Thuan & Lipovetsky (1994). In several cases, the derived value of the extinction $c(\text{H} \beta)$ is negative and is set to zero.

The dereddened line intensities of the H II regions in the final list are given in Table A1 of the Appendix, available on line. The line intensities are given on a scale in which $I(\text{H} \beta) = 1$. The objects are listed in order of right ascension. The first column gives the order number of the ob-

ject. The J2000.0 right ascension and declination of each object are given in columns 2 and 3 respectively. They are the SDSS identifiers of each object. Right ascensions are in units of hours, minutes and seconds and declinations are in units of degrees, arcminutes, and arcseconds. The SDSS spectrum number, (composed of the plate number, the modified Julian date of observations and the number of the fiber on the plate) is listed in column 4. The measured [O II] λ 3727+ λ 3729, [O III] λ 4363, [O III] λ 4959+ λ 5007, [S II] λ 6717, [S II] λ 6731, [O II] λ 7320+ λ 7330 line intensities are given in columns from 5 to 10 respectively.

Our final list includes only high-metallicity objects, those with $12+\log(\text{O}/\text{H}) \gtrsim 8.2$, which gives a total of 181 H II region spectra. (The oxygen abundances were estimated using the measured electron temperatures $t_{3,\text{O}}$ and $t_{2,\text{O}}$.) Several H II regions have repeated observations (7 objects have 2 spectra, and 5 objects have 3 spectra) so that the number of H II regions (164) is less than the number of spectra (181). We have excluded low-metallicity H II regions from the present study for the following reason.

A key part of our analysis rests on the comparison between two $t_{2,\text{O}}-t_{3,\text{O}}$ diagrams, one for SDSS H II regions and the other one for H II regions in nearby galaxies. In a previous study (Pilyugin et al. 2009), we have considered the $t_{2,\text{O}}-t_{3,\text{O}}$ diagram for high-metallicity H II ($12+\log(\text{O}/\text{H}) \gtrsim 8.2$) regions in nearby galaxies. We have fitted the $t_{2,\text{O}}-t_{3,\text{O}}$ relation by the expression of the type

$$t_2 = a_0 + a_1 t_3. \quad (5)$$

The $t_{2,\text{O}}-t_{3,\text{O}}$ diagram exhibits some non-linearity. This non-linearity may be explained in two ways: it is artificial and caused by the linear form adopted for the ff relations for both [O III] and [O II] lines (recall that the ff relation, or the flux-flux relation, links the auroral and nebular oxygen line fluxes in spectra of H II regions). Perhaps a more complex expression may give a better fit to the ff relations. It may also be that the linear expression adopted for the $t_{2,\text{O}}-t_{3,\text{O}}$ relation is not a good approximation, and that an expression of the type,

$$\frac{1}{t_2} = a_0 + a_1 \frac{1}{t_3}, \quad (6)$$

as suggested by Pagel et al. (1992), is more realistic. Thus, the relations derived by Pilyugin et al. (2009) may be considered as a first-order approximation. Extrapolation of the $t_{2,\text{O}}-t_{3,\text{O}}$ relation established for high-metallicity objects ($12+\log(\text{O}/\text{H}) \gtrsim 8.2$) to the low-metallicity range may be unreliable. Therefore, only high-metallicity SDSS H II regions are considered here. The low-metallicity ones will be discussed elsewhere.

The wavelength range of the SDSS spectra is 3800 – 9300Å so that for nearby galaxies with redshift $z \lesssim 0.02$, the [O II] λ 3727+ λ 3729 emission line is out of that range. The absence of this line prevents the determination of the oxygen abundance and hence the use of SDSS spectra of nearby galaxies in our study. Thus, the galaxies in our sample have redshifts ranging between ~ 0.023 and ~ 0.167 , i.e. they are more distant than ~ 100 Mpc.

For comparison with the SDSS H II region sample, we will be using the data for high-metallicity ($12+\log(\text{O}/\text{H}) \gtrsim 8.2$) single H II regions in nearby galaxies for which recent measurements of t_3 and t_2 are available. Such data have

been compiled by Pilyugin et al. (2009). We have added to this compilation the recent spectrophotometric measurements of Bresolin et al. (2009a,b); Esteban et al. (2009); Saviane et al. (2008).

2.2 General properties of the SDSS H II region sample

We now discuss some general characteristics of the SDSS H II region sample.

The intensities of strong, easily measured lines can be used to separate different types of emission-line objects according to their main excitation mechanism. Baldwin, Phillips & Terlevich (1981) have proposed a diagram where the excitation properties of H II regions are studied by plotting the low-excitation [N II] λ 6584/H α line ratio against the high-excitation [O III] λ 5007/H β line ratio. Using this diagnostic diagram, we have excluded all objects above the solid line given by the equation

$$\log([\text{O III}]\lambda 5007/\text{H}\beta) = \frac{0.61}{\log([\text{N II}]\lambda 6584/\text{H}\alpha) - 0.05} + 1.3(7)$$

which separates objects with H II spectra from those containing an AGN (Kauffmann et al. 2003). The SDSS H II regions included in our final list are shown in upper panel of Fig. 1 by open circles. For comparison, the lower panel of Fig. 1 shows a similar diagram for H II regions in nearby galaxies, as compiled by Pilyugin, Vílchez & Contini (2004).

Fig. 2 shows the density-sensitive [S II] λ 6717/[S II] λ 6731 line ratio as a function of the [S II] λ 6717+ λ 6731 emission line fluxes (upper panel) and of the R_3 line fluxes (lower panel). The expected zero density limit ($[\text{S II}]\lambda 6717/[\text{S II}]\lambda 6731 = 1.44$ at $N_e=1 \text{ cm}^{-3}$ with $t_2 = 1.0$), is shown by the solid line. The dashed and dotted lines show respectively the line ratios corresponding to $N_e=100 \text{ cm}^{-3}$ ($[\text{S II}]\lambda 6717/[\text{S II}]\lambda 6731 = 1.29$) and $N_e=200 \text{ cm}^{-3}$ ($[\text{S II}]\lambda 6717/[\text{S II}]\lambda 6731 = 1.18$). All of the H II regions in our final sample have an electron density $N_e \leq 200 \text{ cm}^{-3}$, with the majority of them having $N_e \leq 100 \text{ cm}^{-3}$. They are thus all in the low-density regime, as is typical of the majority of extragalactic H II regions (Zaritsky, Kennicutt & Huchra 1994; Bresolin et al. 2005). A few SDSS H II regions in the original sample had N_e greater than 200 cm^{-3} , but they were excluded from the final sample so that the low-density approximation can be adopted for subsequent analysis. To determine the electron temperature, $N_e=50 \text{ cm}^{-3}$ has been adopted for all the objects in our final sample. In the electron temperature determination, we have assumed that the H II region is homogeneous and that there is no large difference between the electron densities in different ionic zones such as those of the S⁺, O⁺, and O⁺⁺ ions. If this is not the case, the electron temperatures estimated from $N_e(\text{S}^+)$ can have appreciable errors depending on the change of density across the nebula.

Fig. 3 shows the classical diagnostic diagram of [O III] λ 4959+ λ 5007 versus [O II] λ 3727. The open (green) circles represent SDSS H II regions, the open (blue) squares H II regions in nearby galaxies with measured $t_{2,\text{O}}$ and $t_{3,\text{O}}$ temperatures from the sample mentioned above, and the small (red) plus signs H II regions in nearby galaxies (Pilyugin, Vílchez & Contini 2004). The open (black) triangles show H II regions in nearby galaxies (with measured $t_{2,\text{O}}$ temperatures) used for deriving the ff relation for $Q_{2,\text{O}}$

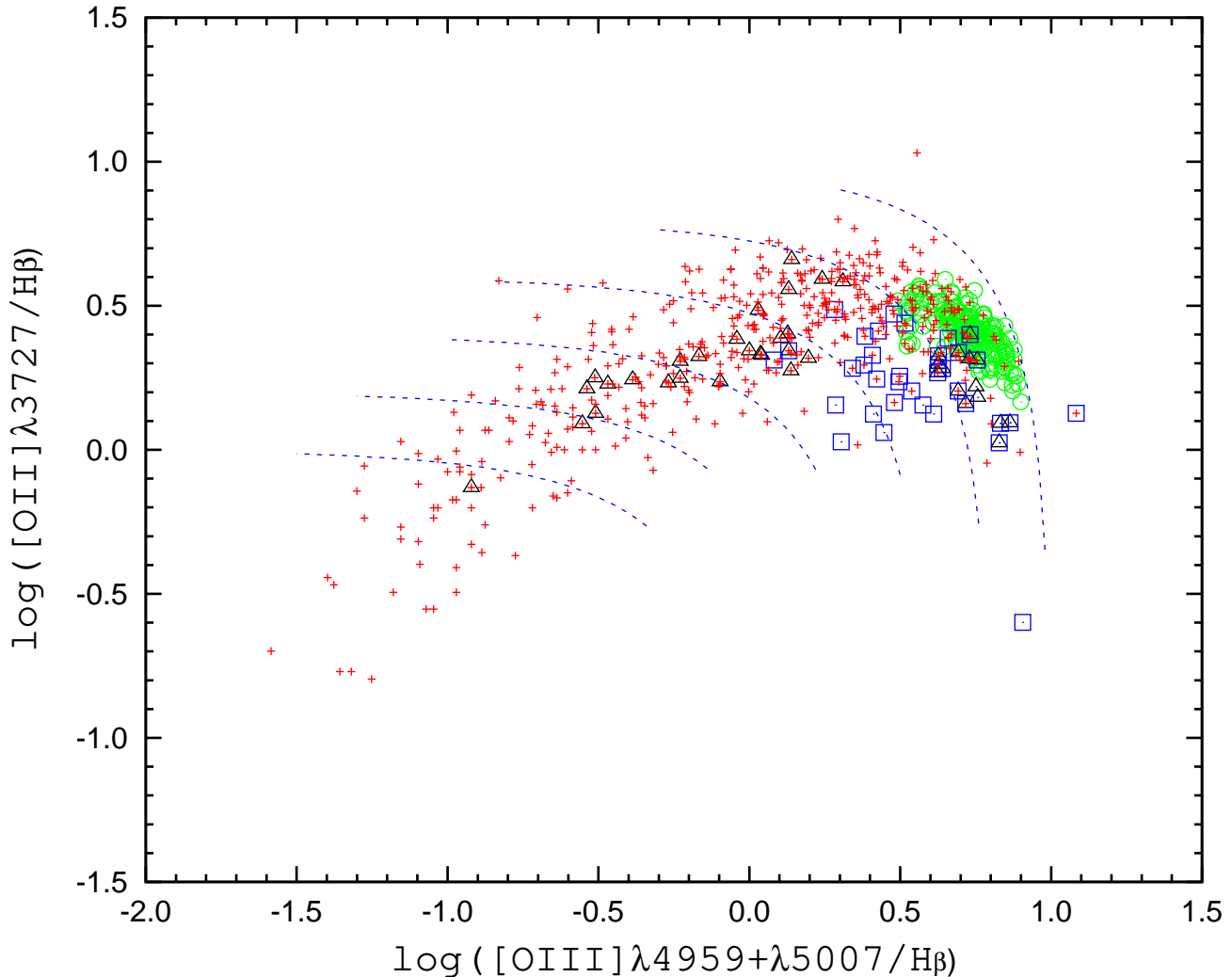


Figure 3. The $[\text{OIII}]\lambda 4959 + \lambda 5007 / \text{H}\beta$ versus $[\text{OIII}]\lambda 3727 / \text{H}\beta$ diagram. The open (green) circles are SDSS H II regions. The open (blue) squares are H II regions in nearby galaxies with measured $t_{2,\text{O}}$ and $t_{3,\text{O}}$ temperatures. The open (black) triangles are H II regions in nearby galaxies used for deriving of the ff relation for $Q_{2,\text{O}}$ in Pilyugin et al. (2009). The small (red) plus signs are H II regions in nearby galaxies (Pilyugin, Vílchez & Contini 2004). The short-dashed lines are lines with $\log R_{23} = 0.0, 0.2, 0.4, 0.6, 0.8, 1.0$ from bottom to top (from left to right). The figure is in colour in the on-line version of the paper.

in Pilyugin et al. (2009). Examination of Fig. 3 shows that the SDSS H II region points fall in the part of the diagram populated by the H II regions in nearby galaxies. This is in agreement with result of Stasińska & Izotov (2003).

An important characteristic of a H II region is the number of the ionizing stars it contains. Under the assumption of an ionization-bounded and dust-free nebula, the H β luminosity provides an estimate of the ionizing flux. The ionizing flux can be expressed in terms of the number of so-called equivalent O stars of a given subtype responsible for producing the ionizing luminosity. The number of zero-age main sequence $O7 V$ stars, $N_{O7 V}$, is usually used to specify the ionizing flux. It can be easily derived from the observed H β luminosity and the Lyman continuum flux of an individual $O7 V$ star. The number of ionizing photons from an $O7 V$ star is taken to be $N_{\text{Lc}} = 5.62 \times 10^{48} \text{ s}^{-1}$ (Martins, Schaerer & Hillier 2005). The distances to SDSS galaxies are calculated using :

$$d = \frac{cz}{H_0}, \quad (8)$$

where d is the distance in Mpc, c the light velocity in km s^{-1} , z the redshift, and H_0 the Hubble constant taken to be equal to $72 (\pm 8) \text{ km s}^{-1} \text{ Mpc}^{-1}$ (Freedman et al. 2001). In general, the H β flux can be affected by underlying absorption and extinction. Underlying absorption is automatically taken into account since we fit the H β line profile with two Gaussians for emission and absorption simultaneously. We do not correct the H β flux for extinction, so the derived numbers of ionizing stars are lower limits. The B magnitude of the SDSS galaxy is obtained from the SDSS m_g and m_r magnitudes from the relation

$$m_B = m_g + 0.42(m_g - m_r) + 0.22, \quad (9)$$

derived from the data of Fukugita et al. (1996). The SDSS galaxies in our sample are shown by filled circles in the $N_{O7 V}$ vs. L_B diagram (Fig. 4). Kennicutt (1988) has given

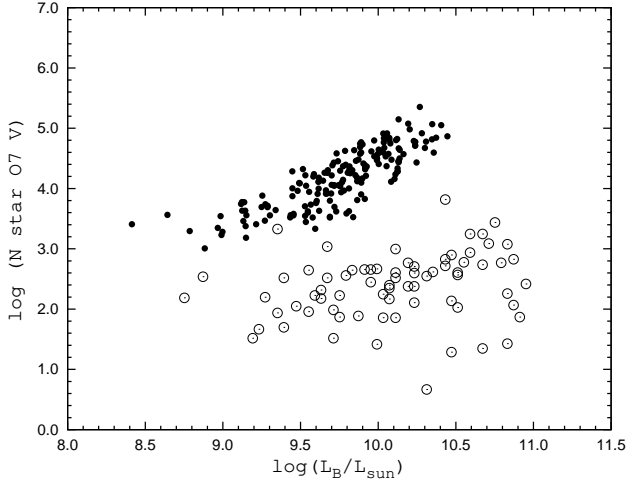


Figure 4. The equivalent number of $O7 V$ stars $N_{O7 V}$ responsible for the excitation of H II regions versus the host galaxy luminosity L_B diagram. The filled circles represent SDSS objects. The open circles show mean values of the three brightest H II regions in nearby galaxies (Kennicutt 1988).

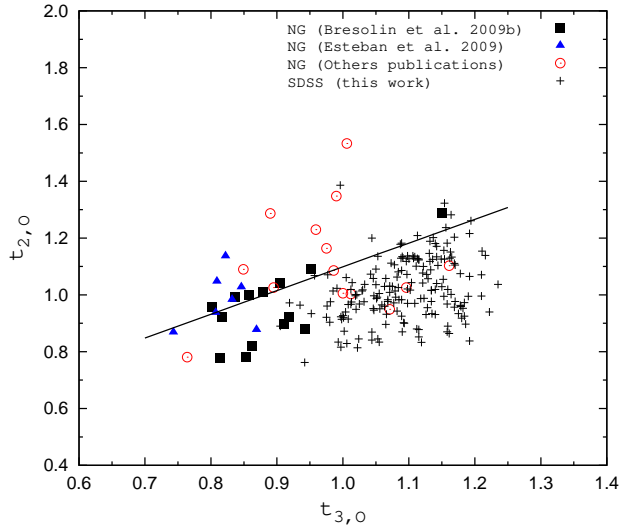


Figure 5. The $t_{2,O} - t_{3,O}$ diagram. The (black) plus signs represent SDSS H II regions. The H II regions in nearby galaxies are shown by filled (black) squares (Bresolin et al. 2009b), filled (blue) triangles (Esteban et al. 2009), and open (red) circles (data from other sources). The solid line shows the $t_{2,O}-t_{3,O}$ relation derived for H II regions in nearby galaxies (Pilyugin et al. 2009). The figure is in colour in the on-line version of the paper.

the mean $H\alpha$ fluxes for the three brightest H II regions in a sample of nearby galaxies. Those fluxes, converted to equivalent numbers of $O7 V$ stars are shown in the same figure by open circles. Fig. 4 shows that the SDSS H II regions contain many more (up to ~ 3 order of magnitude) ionizing stars, when compared to the brightest H II regions in nearby galaxies. This is not a surprising result. On the one hand, the SDSS H II regions suffer from a strong selection effect since, for distant galaxies, the weak $[O III]\lambda 4363$ and $[O II]\lambda 7320+\lambda 7330$ auroral lines are detectable in only very

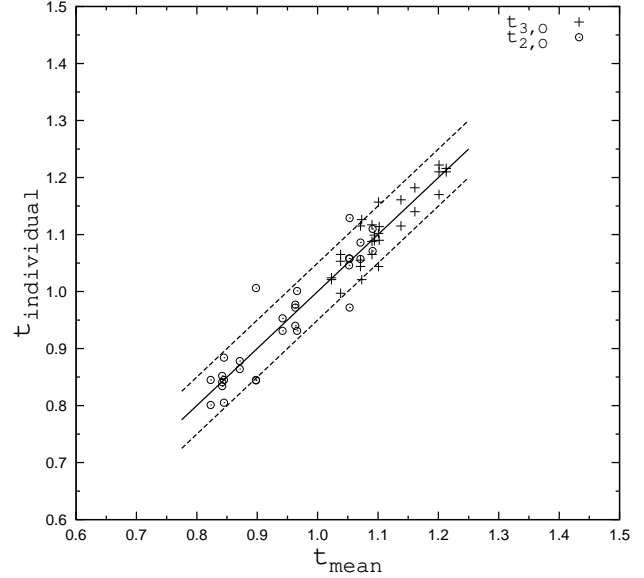


Figure 6. Individual electron temperatures versus average electron temperatures for SDSS H II regions in which electron temperatures have been measured from two or three different spectra. Plus signs show $t_{3,O}$ temperatures, while open circles show $t_{2,O}$ temperatures. The solid line is the locus of equal values, while the dashed lines represent shifts of ± 0.05 along the y-axis.

bright H II regions. On the other hand, the SDSS spectra are obtained through 3-arcsec diameter fibers. The redshifts of our SDSS sample range from ~ 0.025 to ~ 0.17 . At a redshift of $z=0.025$, the projected aperture diameter is ~ 1.5 kpc, while it is ~ 10 kpc at a redshift of $z=0.17$. This suggests that SDSS spectra are closer to global spectra of galaxies, i.e. composite nebulae including multiple star clusters, rather than to spectra of individual H II regions.

3 THE $t_2 - t_3$ DIAGRAM

To convert the quantities $Q_{3,O}$ and $Q_{2,O}$ to the electron temperatures $t_{3,O}$ and $t_{2,O}$, we have used the five-level-atom model, together with recent atomic data for the O^+ and O^{++} ions. The Einstein coefficients of the spontaneous transitions for the five low-lying levels for both ions were taken from Froese Fisher & Tachiev (2004). The energy levels were taken from Edlén (1985) for O^{++} and from Wenåker (1990) for O^+ . The effective cross-sections, or effective collision strengths, for electron impact were taken from Aggarwal & Keenan (1999) for O^{++} and from Pradhan et al. (2006) for O^+ . We have fitted their tabulated data by a second-order polynomial in temperature. The derived $t_{3,O}$ and $t_{2,O}$ are listed respectively in columns 11 and 12 of Table A1 in the Appendix, available on line.

Fig. 5 shows the $t_{2,O}-t_{3,O}$ diagram. The SDSS sample H II regions are shown by (black) plus signs. For comparison, the data for high-metallicity H II regions in nearby galaxies with measured $t_{2,O}$ and $t_{3,O}$ temperatures are also plotted. The data of Bresolin et al. (2009b) are shown by filled (black) squares, that of Esteban et al. (2009) by filled (blue) triangles, and that from other sources (discussed above) by open (red) circles. The solid line is the $t_{2,O}-t_{3,O}$ relation

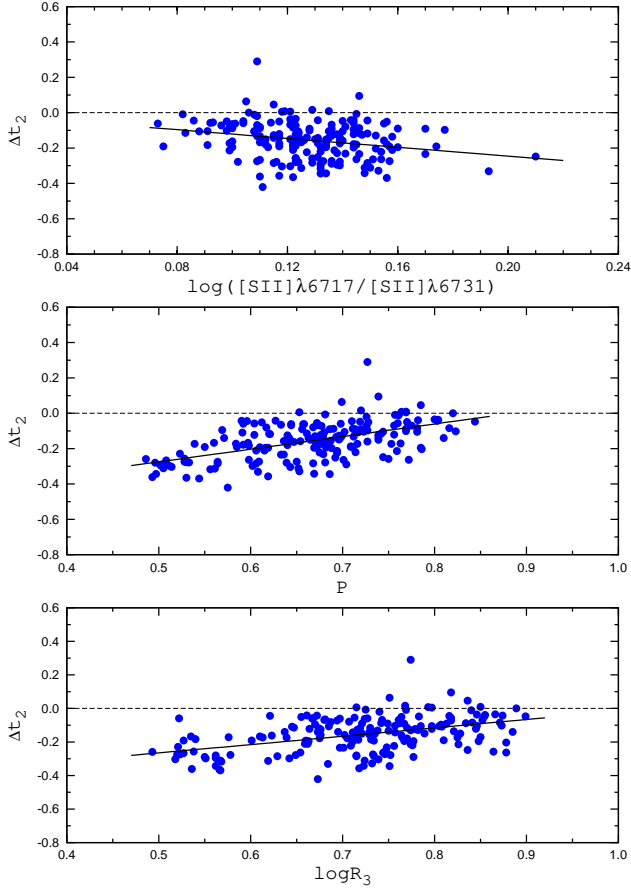


Figure 7. Deviations of $t_{2,O}$ from the $t_{2,O}-t_{3,O}$ relation as a function of the density-sensitive $[\text{S II}]\lambda 6717/[\text{S II}]\lambda 6731$ line ratio (*upper panel*), of the excitation parameter P (*middle panel*), and of the R_3 line flux (*bottom panel*). The solid lines show the obtained correlations, Table 1.

derived for H II regions in nearby galaxies (Pilyugin et al. 2009). It is of the form:

$$t_{2,O} = 0.835 t_{3,O} + 0.264 \quad (10)$$

Fig. 5 shows that some H II regions lie above that relation. It has been found (Pilyugin et al. 2009) that H II regions with strong nebular R_3 line fluxes do not follow the $t_{2,O}-t_{3,O}$ relation: they are shifted towards higher $t_{2,O}$ temperatures. This shift can be caused by the fact that the low-lying metastable levels in some ions can be excited not only by the electron collisions, but also by recombination processes (Rubin 1986; Liu et al. 2000; Stasińska 2005). Since recombination-excited emission of $[\text{O II}]\lambda 7325$ radiation will occur in the O^{++} zone, the effect on the collision-excited lines will depend on the R_3 line flux. As a result, one may expect a significant shift toward higher values of $t_{2,O}$ for H II regions with strong R_3 line fluxes.

Examination of Fig. 5 clearly shows that there is a large scatter of $t_{2,O}$ for a given $t_{3,O}$. Moreover, the majority of the SDSS H II regions lie below the $t_{2,O}-t_{3,O}$ relation established for H II regions in nearby galaxies. Although the SDSS H II regions have strong nebular R_3 line fluxes, they lie below, not above the solid line as the H II regions with strong nebular R_3 line fluxes in nearby galaxies. In conjunction with the

Table 1. The coefficients a_0 and a_1 in the relations $\Delta t_2 = a_0 + a_1 X$, Eq. (11), and the values of the correlation coefficient.

X	a_0	a_1	correlation coefficient
$\log([\text{S II}]\lambda 6717/[\text{S II}]\lambda 6731)$	0.00	-1.24	-0.25
P	-0.63	0.71	0.55
$\log(R_3)$	-0.51	0.50	0.45

lower $t_{2,O}$ temperatures, the SDSS H II regions show also a shift towards higher $t_{3,O}$ temperatures.

Can uncertainties in the electron temperatures measurements be responsible for the observed scatter and shift of the SDSS H II regions in the $t_{2,O}-t_{3,O}$ diagram? We noted above that several SDSS H II regions possess two or three individual spectra with measurable temperature-sensitive nebular to auroral $Q_{2,O}$ and $Q_{3,O}$ line ratios. Comparison between separate measurements of the electron temperatures for the same H II region can give us an indication of their accuracies. In Fig. 6, we have plotted the individual value of the electron temperature versus the average value for SDSS H II regions that have electron temperatures measured separately from two or three spectra. The plus signs show $t_{3,O}$ temperatures, and the open circles $t_{2,O}$ temperatures. The solid line is the line of equal values and the dashed lines show shifts of ± 0.05 along the y-axis. Inspection of Fig. 6 shows that the typical scatter between individual measurements of both $t_{2,O}$ and $t_{3,O}$ is usually less than ~ 1000 K. This can be considered as an estimate of the uncertainties in the electron temperature measurements. Then, these uncertainties are considerably less than the observed scatter and shift of the SDSS H II regions in the $t_{2,O}-t_{3,O}$ diagram.

We define the deviation $\Delta t_{2,O}$ of $t_{2,O}$ from the $t_{2,O}-t_{3,O}$ relation as the difference between the measured $t_{2,O}$ and that obtained from the $t_{2,O}-t_{3,O}$ relation for a given $t_{3,O}$. Fig. 7 shows $\Delta t_{2,O} = t_{2,O} - t_{2,O}^r$ as a function of the density-sensitive $[\text{S II}]\lambda 6717/[\text{S II}]\lambda 6731$ line ratio (*upper panel*), of the excitation parameter P (*middle panel*), and of the R_3 line flux (*lower panel*). The correlations of $\Delta t_{2,O}$ with different parameters were examined by obtaining relations of the type

$$\Delta t_{2,O} = a_0 + a_1 X \quad (11)$$

where X is successively $\log([\text{S II}]\lambda 6717/[\text{S II}]\lambda 6731)$, P , and $\log(R_3)$. The derived coefficients a_0 and a_1 and the correlation coefficients are given in Table 1. The derived relations are shown in Fig. 7 by solid lines. It is seen that the deviations $\Delta t_{2,O}$ do not correlate strongly with electron density, but do show some weak correlation (the correlation coefficient is ~ 0.5) with P and R_3 .

4 ON A POSSIBLE ORIGIN OF THE SCATTER IN THE $t_2 - t_3$ DIAGRAM

We have remarked above that that the spectra of the SDSS H II regions correspond more to those of composite nebulae than to those of individual H II regions. Can this be responsible for the scatter and shift of the SDSS H II regions relative to the $t_{2,O}-t_{3,O}$ relation?

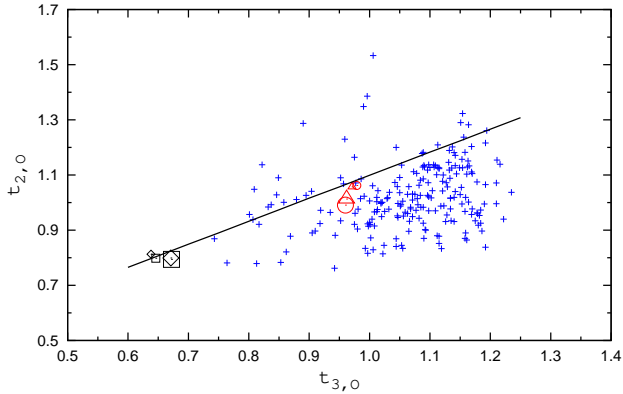


Figure 8. The $t_{2,O}-t_{3,O}$ diagram for observed and modeled (Ercolano, Bastian & Stasińska 2007) H II regions. The SDSS and nearby H II regions are shown by plus signs. The key for the model symbols is given in Table 2. The solid line shows the $t_{2,O}-t_{3,O}$ relation derived for H II regions in nearby galaxies (Pilyugin et al. 2009). The figure is in colour in the on-line version of the paper.

Table 2. Key for the symbols representing the Ercolano, Bastian & Stasińska (2007) models in Fig. 8.

Symbol	star distrib.	geometry	Z/Z_{\odot}	model
small black rhomb	central	sphere	1.0	CSp1.0
large black rhomb	distrib.	sphere	1.0	FSp1.0
small black square	central	shell	1.0	CSh1.0
large black square	distrib.	shell	1.0	FSh1.0
small red circle	central	sphere	0.4	CSp0.4
large red circle	distrib.	sphere	0.4	FSp0.4
small red triangle	central	shell	0.4	CSh0.4
large red triangle	distrib.	shell	0.4	FSh0.4

Ercolano, Bastian & Stasińska (2007) have shown that the temperature structure of models with centrally concentrated ionizing sources may be quite different from those of models where the ionizing sources are randomly distributed within the volume, with generally non-overlapping Strömgren spheres. These differences may contribute to the scatter the $t_{2,O} - t_{3,O}$ diagram. The models of Ercolano, Bastian & Stasińska (2007) are shown along with the SDSS and nearby galaxy samples in the $t_{2,O}-t_{3,O}$ diagram in Fig. 8. The key for the different model symbols is given in Table 2. Examination of Fig. 8 shows that the positions of the composite nebulae, consisting of several distributed H II regions, are indeed shifted lower relatively to the positions of the single nebulae. However, the predicted shift is considerably smaller than the observed shifts of the SDSS and nearby galaxy data points (plus signs).

The composite nebula can be ionised by sources of different temperatures. Ercolano, Bastian & Stasińska (2007) have considered the case of an ionising set composed of two stellar populations, a $37 M_{\odot}$ and a $56 M_{\odot}$ composed, with half of the ionising photon being emitted by each population. These masses correspond to stars of spectral types O5 and O3 respectively (Martins, Schaerer & Hillier 2005). However, those authors did not consider the case of a single

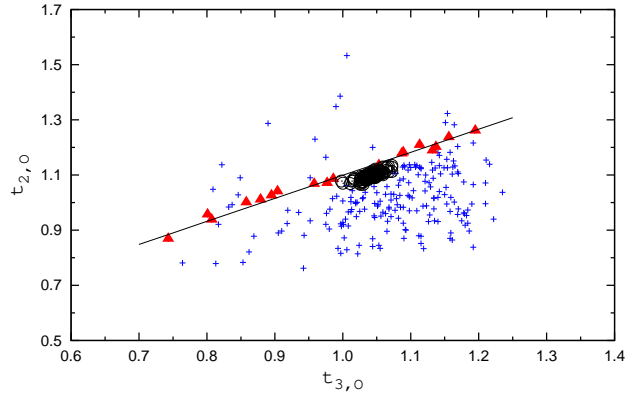


Figure 9. The $t_{2,O} - t_{3,O}$ diagram. Open (black) circles represent artificial composite H II regions consisting of randomly scaled components (shown by filled (red) triangles). Plus (blue) signs show SDSS and nearby H II regions. The continuous line is the $t_{2,O}-t_{3,O}$ relation (Pilyugin et al. 2009). The figure is in colour in the on-line version of the paper.

stellar population, so that a direct comparison between the ionisation structure produced by single and composite populations is not possible. We have performed Monte Carlo runs to model the temperature shifts from the $t_{2,O}-t_{3,O}$ relation caused by having several ionizing sources with different temperatures within the same aperture in the following way. We have assumed that each SDSS H II region consists of several components, with every component following the $t_{2,O}-t_{3,O}$ relation. These components are shown by filled (red) triangles in Fig. 9.

If the H II region line fluxes are given on a scale where $F(\text{H}\beta)=1$, then the total $F(\text{H}\beta)$ flux of the composite H II region is given by the expression:

$$F(\text{H}\beta) = \sum_{j=1}^{j=n} w_j \quad (12)$$

and the flux $F(X_{\lambda_k})$ of the composite H II region in the line X_{λ_k} is given by:

$$F(X_{\lambda_k}) = \frac{\sum_{j=1}^{j=n} w_j F_j(X_{\lambda_k})}{\sum_{j=1}^{j=n} w_j} \quad (13)$$

where n is the number of components in the composite H II region, which we take to be equal to 18, and w_j are numbers between 0 and 1 produced by a random number generator.

We have performed 100 Monte Carlo runs, producing in each run an artificial spectrum of composite H II regions. For every computed spectrum, we have estimated the electron temperatures $t_{2,O}$ and $t_{3,O}$. The positions of those artificial composite H II regions in the $t_{2,O}-t_{3,O}$ diagram are shown by open (black) circles in Fig. 9. The model points are shifted below the solid line, but again the shift is rather small.

We next decrease the number of components to 3, with each component being widely separated in temperature from the others. They are shown by (red) triangles in the top panel of Fig. 10. We have computed 200 artificial spectra of composite H II regions. Like before, the contribution of

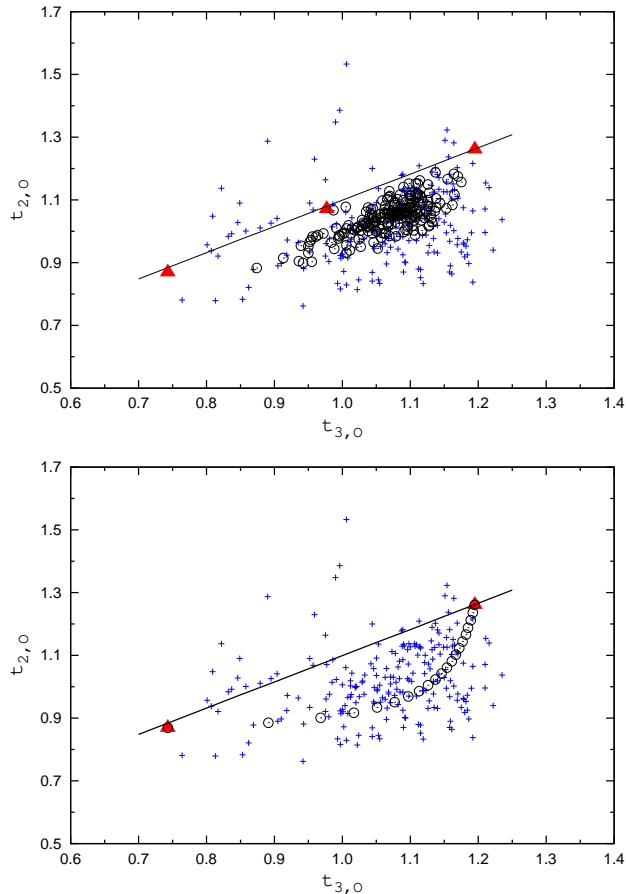


Figure 10. The same as Fig. 9, but for three-component (*top panel*) and two-component (*bottom panel*) composite H II regions.

each component is randomly scaled. The positions of those artificial spectra in the $t_{2,O}$ – $t_{3,O}$ diagram are shown by the open (black) circles in the top panel of Fig. 10. It is seen that, in this case, there are composite H II regions that are significantly shifted below the $t_{2,O}$ – $t_{3,O}$ relation, although they still cannot match the positions of the SDSS H II regions with the largest shifts.

We next compute artificial spectra of two-component H II regions. These are shown in the $t_{2,O}$ – $t_{3,O}$ diagram by open (black) circles in the bottom panel of Fig. 10. In this case, w_1 and w_2 are not random numbers, but are chosen so that w_1 varies from 0 to 1 with a step of 0.05 and $w_2 = 1 - w_1$. Again, those composite H II regions are significantly shifted from the $t_{2,O}$ – $t_{3,O}$ relation, although they again do not reproduce the positions of the SDSS objects with the largest shifts. However, examination of Fig. 10 suggests that the SDSS objects with the largest shifts, if real, can be reproduced by a composite object where the hot component has $t_{2,O} \sim 1.3$ and the cool component $t_{2,O} \sim 0.8$. Unfortunately, we cannot test directly this expectation since the data for an actual H II region with both $t_{2,O}$ and $t_{3,O}$ measured, which follows the $t_{2,O}$ – $t_{3,O}$ relation, and with $t_{2,O} \sim 0.8$ is not available.

In summary, the observed $t_{2,O}$ – $t_{3,O}$ diagram can be understood if the SDSS H II regions are composites of a few H II regions with different emission line properties. The evo-

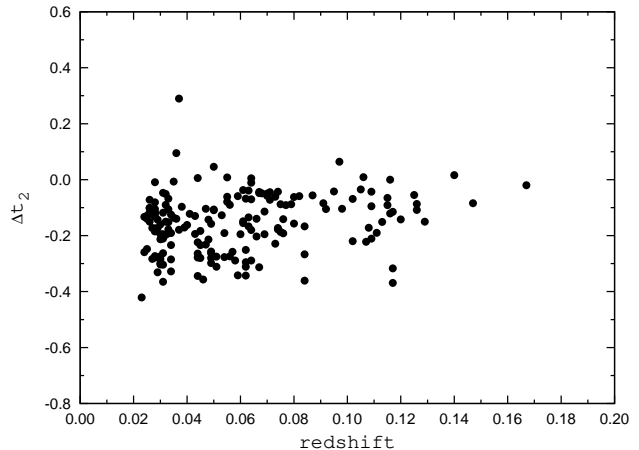


Figure 11. Deviations of $t_{2,O}$ from the $t_{2,O}$ – $t_{3,O}$ relation as a function of redshift.

lution of H II regions associated with stars and star clusters has been considered in many papers (Stasińska 1978, 1980; McCall, Rybski & Shields 1985; Dopita & Evans 1986; Moy, Rocca-Volmerrange & Fioc 2001; Stasińska & Izotov 2003; Dopita et al. 2006, among others). It is well established that the H II region spectral sequence depends on three fundamental parameters: the metallicity, the ionizing star cluster spectral energy distribution and the ionization parameter. Ercolano, Bastian & Stasińska (2007) have shown that variations in the ionization parameter cannot be the main reason for the scatter in the $t_{2,O}$ – $t_{3,O}$ diagram. Variations of the ionizing star cluster spectral energy distribution are governed by two independent parameters: age and metallicity. Then, the shifted SDSS H II regions should consist of components of different ages or/and different metallicities.

Of these two parameters, which is mainly responsible for the differences in the emission line properties of the components of the SDSS H II regions? Because of radial abundance gradients in the disks of spiral galaxies, the oxygen abundances in H II regions near the center of a galaxy and those at the periphery can differ by up to an order of magnitude (Pilyugin, Vílchez & Contini 2004). We noted above that the SDSS spectra are obtained through 3-arcsec diameter fibers, and the projected aperture diameter increases with redshift, up to ~ 10 kpc at the redshift of $z = 0.17$. The range of galactocentric distances and, consequently, the range of metallicities of H II regions which contribute to the SDSS spectra, is larger for distant than for nearby galaxies. If metallicity variations are responsible for the differences in the emission line properties of the H II regions which contribute to the SDSS spectra, then the deviations of these H II regions from the $t_{2,O}$ – $t_{3,O}$ relation should increase with redshift. In Fig. 11, we plot the deviations $\Delta t_{2,O}$ of the SDSS objects as a function of redshift. There is not a significant correlation.

This suggests that age is the main factor of the scatter of the SDSS H II regions rather than metallicity. It should be noted, however, that the evolution of H II regions associated with star clusters is generally accompanied by a variation of its chemical composition through a self-enrichment process (Kunth & Sargent 1986; Pilyugin 1992, 1993). Then

young and old H II regions can have different chemical compositions. However these chemical differences are not seen in optical spectra of H II regions that are only several million years old. Thus, we conclude that it is the differences in the ionizing star cluster spectral energy distributions, caused by their age variations, that are responsible for the differences in the emission-line properties of the H II regions in SDSS galaxies.

Our explanation of the observed scatter and shift of the SDSS H II regions in the $t_{2,O}-t_{3,O}$ diagram is based on the hypothesis that SDSS spectra result from a mix of H II regions ionized by sources of different temperatures. This hypothesis is in line with results derived from considerations of other diagrams. Stasińska & Izotov (2003) have noted that the classical diagnostic diagram $[\text{O III}]\lambda 4959 + \lambda 5007$ versus $[\text{O II}]\lambda 3727$ is not completely understood in terms of pure photoionization models. Stasińska, Schaerer & Leitherer (2001) have proposed an additional heating mechanism to account for the largest $[\text{O II}]\lambda 3727$ observed fluxes. Moy, Rocca-Volmerrange & Fioc (2001) have concluded that the best fits of emission-line ratios in starburst and H II galaxies are obtained with a combination of a high- and low-ionization components. In terms of the present study, those conclusions mean that giant H II objects with the largest $[\text{O II}]\lambda 3727$ fluxes are composite H II regions.

Dopita et al. (2006) have modeled a H II region associated with star clusters where stars are being formed continuously. They have computed line flux-averaged spectra along evolutionary tracks of H II regions, and have found that the older evolved H II regions make a significant contribution to the low-ionization lines (e.g. $[\text{O II}]\lambda 3727$), while high-ionization lines, such as $[\text{O III}]\lambda 4959 + \lambda 5007$, will be mostly produced in the very youngest H II regions. In the light of our present results, one can expect the following picture for the models of Dopita et al. (2006). Continuous star formation can be considered as a sequence of many substarbursts of different ages, i.e. as a sequence of many ionizing sources with different spectral energy distributions. If all the substarbursts have a similar amplitude, i.e. if there are no large variations in the star formation rate, then the associated H II regions will lie close to the $t_{2,O}-t_{3,O}$ relation (Fig. 9). On the other hand, if a few substarbursts have a significantly higher amplitude, i.e. if the star formation rate varies appreciably, then the associated H II regions will show significant deviations from the $t_{2,O}-t_{3,O}$ relation (Fig. 10).

To summarize, the presence of low-ionization components in giant H II regions appears to be substantiated by a number of different investigations. However, their origin is not yet clear. Are they old and cold H II regions as suggested by Dopita et al. (2006), or are they the “low-ionization components excited by an additional heating mechanism” as suggested by Stasińska, Schaerer & Leitherer (2001), or are they the diffuse ionized medium? A detailed study of very cold H II regions can clarify this matter.

5 CONCLUSIONS

Spectra of H II regions where the two auroral $[\text{O III}]\lambda 4363$ and $[\text{O II}]\lambda 7325$ lines are detectable have been visually extracted from the Data Release 6 of the Sloan Digital Sky Survey (SDSS). Our final list consists of 181 spectra of high-

metallicity ($12 + \log(\text{O}/\text{H}) \gtrsim 8.2$) SDSS H II regions. The redshifts of our SDSS sample lie in the range from ~ 0.025 to ~ 0.17 . The SDSS H II regions fall in the region in the classical $[\text{O III}]\lambda 4959 + \lambda 5007$ versus $[\text{O II}]\lambda 3727$ diagnostic diagram populated by the H II regions of nearby galaxies. At the same time, the number of equivalent $O7 V$ stars in the H II regions of the SDSS sample is considerably larger (up to three orders of magnitude) than that in the brightest H II regions in nearby galaxies.

The $t_{2,O}-t_{3,O}$ diagram for the SDSS sample is examined. It is found that there is a large scatter of the $t_{2,O}$ electron temperature, for a given $t_{3,O}$ electron temperature. The majority of the SDSS H II regions lie below the $t_{2,O}-t_{3,O}$ relation obtained for H II regions in nearby galaxies, i.e. they show a systematic shift towards lower $t_{2,O}$ temperatures or/and towards higher $t_{3,O}$ temperatures.

The observed scatter and shift of the SDSS H II regions in the $t_{2,O}-t_{3,O}$ diagram can be explained if the SDSS spectra correspond to a mix of H II regions ionized by sources of different temperatures. The sources of ionization can be centrally concentrated or distributed within the H II region volume. In the latter case, there is an additional scatter as found by Ercolano, Bastian & Stasińska (2007).

ACKNOWLEDGMENTS

We are grateful to the referee of this paper for his/her constructive comments. L.S.P. thanks the staff of the Instituto de Astrofísica de Andalucía for hospitality during a visit when a significant part of this investigation was carried out. T.X.T thanks the financial support of NSF and NASA.

REFERENCES

- Aggarwal K.M., Keenan F.P., 1999, ApJS, 123, 31
- Baldwin J.A., Phillips M.M., Terlevich R. 1981, PASP, 93, 5
- Bresolin F., Schaerer D., Conzález Delgado R.M., Stasińska G., 2005, A&A, 441, 981
- Bresolin F., Ryan-Weber E., Kennicutt R.C., Goddard Q., 2009a, ApJ, 695, 580
- Bresolin F., Gieren W., Kudritzki R.-P., Pietrzyński G., Urbaneja M.A., Carraro G., 2009b, ApJ, 700, 309
- Campbell A., Terlevich R., Melnick J., 1986, MNRAS, 223, 811
- Deharveng L., Peña M., Caplan J., Costero R., 2000, MNRAS, 311, 329
- Dopita M.A., Evans I.N., 1986, ApJ, 307, 431
- Dopita M.A., Fischera J., Sutherland R.S., et al., 2006, ApJS, 167, 177
- Edlén B., 1985, Phys. Scripta, 31, 345
- Ercolano B., Bastian N. & Stasińska G., 2007, MNRAS, 379, 945
- Esteban C., Bresolin F., Peimbert M., Carcía-Rojas J., Peimbert A., Mesa-Delgado A., 2009, ApJ, 700, 654
- Freedman W.L., Madore B.F., Gibson B.K., et al., 2001, ApJ, 553, 47
- Froese Fischer C., Tachiev G., 2004, ADNDT, 87, 1
- Fukugita M., Ichikawa T., Gunn J.E., Doi M., Shimasaku K., Schneider D.P., 1996, AJ, 111, 1748

Izotov Y.I., Thuan T.X., Lipovetsky V.A., 1994, ApJ, 435, 647

Izotov Y.I., Thuan T.X., Lipovetsky V.A., 1997, ApJS, 108, 1

Izotov Y.I., Stasińska G., Meynet G., Guseva N.G., Thuan T.X., 2006, A&A, 448, 955

Garnett D.R. 1992, AJ, 103, 1330

Hägele G.F., Pérez-Montero E., Díaz Á.I., Terlevich E., Terlevich R., 2006, MNRAS, 372, 293

Hägele G.F., Díaz Á.I., Terlevich E., Terlevich R., Pérez-Montero E., Cardaci M.V., 2008, MNRAS, 383, 209

Kauffmann G., Heckman T.M., Tremonti C., et al. 2003, MNRAS, 346, 1055

Kennicutt R.C., 1988, ApJ, 334, 144

Kennicutt R.C., Bresolin F., Garnett D. 2003, ApJ, 591, 801

Kunth D., Sargent W.L.W., 1986, ApJ, 300, 496

Liu X.-W., Storey P.J., Barlow M.J., Danziger I.J., Cohen M., Bryce M., 2000, MNRAS, 312, 585

Martins F., Schaerer D., Hillier D.J., 2005, A&A, 436, 1049

McCall M.L., Rybski P.M., Shields G.A., 1985, ApJS, 57, 1

Moy E., Rocca-Volmerange B., Fioc M., 2001, A&A, 365, 347

Oey M.S., Shields M.G., 2000, ApJ, 539, 687

Pagel B.E.J., Simonson E.A., Terlevich R.J., Edmunds M.G., 1992, MNRAS, 255, 325

Pettini M., Pagel B.E.J., 2004, MNRAS, 348, 59L

Pilyugin L.S., 1992, A&A, 260, 58

Pilyugin L.S., 1993, A&A, 277, 42

Pilyugin L.S., 2000, A&A, 362, 325

Pilyugin L.S., 2001, A&A, 369, 594

Pilyugin L.S., 2003, A&A, 399, 1003

Pilyugin L.S., 2007, MNRAS, 375, 685

Pilyugin L.S., Mattsson L., Vílchez J.M., & Cedrés B., 2009, MNRAS, 398, 485

Pilyugin L.S., Thuan T.X., 2005, ApJ, 631, 231

Pilyugin L.S., Thuan T.X., 2007, ApJ, 669, 290

Pilyugin L.S., Vílchez J.M., Contini T., 2004, A&A, 425, 849

Pilyugin L.S., Vílchez J.M., Thuan T.X., 2006, MNRAS, 370, 1928

Pradhan A.K., Montenegro M., Nahar S.N., Eissner W., 2006, MNRAS, 366, L6

Rubin R.H., 1986, ApJ, 309, 334

Saviane I., Ivanov V.D., Held E.V., Alloin D., Rich R.M., Bresolin F., Rizzi L., 2008, A&A, 487, 901

Stasińska G., 1978, A&A, 66, 257

Stasińska G., 1980, A&A, 84, 320

Stasińska G., 1982, A&AS, 48, 299

Stasińska G., 1990, A&AS, 83, 501

Stasińska G., 2005, A&A, 434, 507

Stasińska G., Izotov Y., 2003, A&A, 397, 71

Stasińska G., Schaerer D., 1997, A&A, 322, 615

Stasińska G., Schaerer D., Leitherer C., 2001, A&A, 370, 1

Wenåker I., 1990, Phys. Scripta, 42, 667

Zaritsky D., Kennicutt R.C., Huchra J.P., 1994, ApJ, 420, 87

APPENDIX A: ONLINE MATERIAL. TABLE A1.

Table A1 contains the dereddened line intensities and the electron temperatures of the SDSS H II regions. The line intensities are given on a scale in which $H\beta = 1$. The objects are listed in order of right ascension. The first column gives the order number of the object. The J2000.0 right ascension and declination of each object are given in columns 2 and 3 respectively. They constitute the SDSS identifier of each object. Units of right ascension are hours, minutes, and seconds and units of declination are degrees, arcminutes, and arcseconds. The SDSS spectrum number, composed of the plate number, the modified Julian date of observations and the number of the fiber on the plate, is given in column 4. The measured $[O\ II]\lambda 3727 + \lambda 3729$, $[O\ III]\lambda 4363$, $[O\ III]\lambda 4959 + \lambda 5007$, $[S\ II]\lambda 6717$, $[S\ II]\lambda 6731$, $[O\ II]\lambda 7320 + \lambda 7330$ line intensities are listed in columns from 5 to 10 respectively. The derived electron temperatures $t_{3,O}$ and $t_{2,O}$ are given in columns 11 and 12 respectively.

Table A1. Dereddened line intensities and electron temperatures of a sample of HII regions in SDSS galaxies. The line intensities are given on a scale in which $H\beta=1$.

No ^a	RA ^b	DEC ^c	Spectrum ^d number	[O II] $\lambda 3727$	[O III] $\lambda 4363$	[O III] $\lambda 4959+\lambda 5007$	[S II] $\lambda 6717$	[S II] $\lambda 6731$	[O II] $\lambda 7325$	t _{3,O}	t _{2,O}
1	00 06 57.01	00 51 26.0	686 52519 406	1.840	0.0619	7.477	0.173	0.128	0.0478	1.192	1.216
2	00 20 12.06	-00 43 06.3	1088 52929 183	2.675	0.0283	5.538	0.230	0.174	0.0537	1.014	1.043
3	00 51 18.38	00 32 57.7	394 51913 469	3.530	0.0262	3.432	0.303	0.235	0.0493	1.158	0.870
4	00 51 18.38	00 32 57.7	691 52199 626	2.693	0.0226	3.425	0.303	0.227	0.0516	1.102	1.017
5	00 51 18.38	00 32 57.7	394 51812 466	3.262	0.0189	3.367	0.295	0.229	0.0454	1.044	0.869
6	00 52 33.72	00 19 52.6	394 51913 493	3.609	0.0204	3.645	0.346	0.252	0.0467	1.044	0.841
7	00 52 33.72	00 19 52.6	394 51876 494	3.690	0.0250	3.650	0.361	0.265	0.0491	1.115	0.852
8	00 52 33.72	00 19 52.6	394 51812 487	3.617	0.0213	3.688	0.356	0.252	0.0459	1.055	0.834
9	01 32 58.54	-08 53 37.8	662 52147 466	2.725	0.0227	4.582	0.356	0.256	0.0564	1.005	1.061
10	02 11 59.94	-01 13 02.8	405 51816 365	3.481	0.0389	4.708	0.302	0.234	0.0447	1.192	0.838
11	02 53 25.28	-00 13 56.6	409 51871 033	2.690	0.0425	5.416	0.210	0.156	0.0458	1.169	0.957
12	03 26 14.50	-00 12 10.8	712 52179 156	3.114	0.0173	3.296	0.313	0.237	0.0373	1.022	0.814
13	03 26 14.50	-00 12 10.8	712 52199 158	2.980	0.0176	3.331	0.303	0.223	0.0390	1.024	0.845
14	03 27 50.15	01 01 35.0	414 51869 524	3.268	0.0299	4.700	0.326	0.234	0.0753	1.088	1.129
15	03 27 50.15	01 01 35.0	414 51901 546	2.990	0.0316	4.592	0.338	0.255	0.0541	1.118	0.987
16	03 27 50.15	01 01 35.0	805 52586 550	3.538	0.0278	4.674	0.344	0.247	0.0728	1.065	1.058
17	03 33 14.42	00 24 37.2	713 52178 481	3.711	0.0176	3.647	0.329	0.248	0.0447	0.997	0.816
18	03 33 14.42	00 24 37.2	415 51810 486	3.397	0.0205	3.559	0.328	0.238	0.0444	1.053	0.845
19	03 33 14.42	00 24 37.2	415 51879 497	3.093	0.0206	3.454	0.340	0.256	0.0460	1.065	0.896
20	07 29 30.29	39 49 41.6	1733 53047 528	2.590	0.0364	5.778	0.229	0.182	0.0554	1.084	1.081
21	07 48 06.30	19 31 46.9	1582 52939 335	2.381	0.0274	5.380	0.197	0.148	0.0421	1.013	0.975
22	07 49 15.48	22 53 42.1	1203 52669 570	3.214	0.0426	5.222	0.279	0.213	0.0479	1.186	0.897
23	07 53 32.81	46 44 39.6	1737 53055 555	2.602	0.0474	6.050	0.295	0.208	0.0583	1.169	1.111
24	08 00 00.69	27 46 42.0	859 52317 070	2.197	0.0532	7.076	0.192	0.141	0.0450	1.152	1.055
25	08 06 19.49	19 49 27.3	1922 53315 588	2.167	0.0331	5.801	0.208	0.159	0.0471	1.050	1.091
26	08 08 24.94	23 08 40.8	1584 52943 372	2.985	0.0272	5.352	0.245	0.188	0.0519	1.012	0.967
27	08 14 20.78	57 50 08.0	1872 53386 526	2.532	0.0287	5.091	0.285	0.206	0.0521	1.046	1.058
28	08 20 09.11	23 39 19.6	1926 53317 369	2.655	0.0284	5.263	0.216	0.160	0.0470	1.032	0.976
29	08 23 54.96	28 06 21.6	1267 52932 384	1.964	0.0358	5.716	0.186	0.145	0.0408	1.082	1.063
30	08 24 53.13	39 06 39.1	894 52615 185	2.192	0.0535	6.689	0.186	0.142	0.0464	1.178	1.075
31	08 25 27.65	29 57 39.2	1207 52672 506	3.054	0.0236	4.417	0.357	0.261	0.0582	1.029	1.014
32	08 25 59.30	21 35 46.9	1927 53321 560	2.873	0.0331	4.605	0.361	0.250	0.0549	1.134	1.016
33	08 26 30.79	22 14 24.0	1927 53321 570	2.941	0.0271	4.351	0.357	0.259	0.0537	1.080	0.992
34	08 31 56.33	43 36 12.7	762 52232 224	2.873	0.0418	6.007	0.251	0.189	0.0610	1.121	1.077
35	08 33 26.07	21 51 46.3	1929 53349 100	2.348	0.0287	4.958	0.249	0.187	0.0440	1.055	1.005
36	08 33 43.89	43 19 51.7	762 52232 217	3.019	0.0274	4.612	0.337	0.242	0.0592	1.063	1.030
37	08 37 11.33	23 11 58.1	1929 53349 593	2.731	0.0483	5.846	0.282	0.208	0.0569	1.192	1.065
38	08 38 43.63	38 53 50.5	828 52317 148	1.946	0.0535	6.927	0.188	0.142	0.0463	1.163	1.151
39	08 44 14.22	02 26 21.2	564 52224 216	1.680	0.0545	7.430	0.137	0.109	0.0390	1.142	1.134
40	08 45 27.60	53 08 52.9	447 51877 361	2.231	0.0621	7.546	0.162	0.116	0.0410	1.190	0.995
41	08 45 47.17	27 54 24.5	1588 52965 073	2.829	0.0421	5.301	0.284	0.202	0.0459	1.175	0.934
42	08 56 17.61	26 40 12.7	1933 53381 460	2.347	0.0396	5.852	0.250	0.169	0.0518	1.111	1.101
43	09 04 03.59	36 39 14.2	1212 52703 388	2.512	0.0479	5.978	0.238	0.174	0.0430	1.179	0.959
44	09 04 18.11	26 01 06.3	1935 53387 204	2.691	0.0545	7.022	0.195	0.158	0.0624	1.165	1.133
45	09 07 04.89	53 26 56.6	553 51999 342	2.182	0.0380	5.813	0.223	0.162	0.0421	1.098	1.021
46	09 08 00.08	50 39 10.0	552 51992 027	2.934	0.0421	5.191	0.286	0.215	0.0516	1.184	0.973
47	09 12 52.31	50 26 21.3	766 52247 434	2.868	0.0302	4.522	0.341	0.238	0.0669	1.106	1.137
48	09 14 00.36	49 59 30.9	766 52247 225	3.272	0.0247	3.994	0.360	0.241	0.0575	1.077	0.972
49	09 18 20.53	49 06 34.9	900 52637 388	2.313	0.0358	5.338	0.248	0.178	0.0533	1.107	1.129
50	09 20 33.22	31 36 35.5	1938 53379 406	2.531	0.0464	6.494	0.246	0.183	0.0574	1.132	1.118
51	09 28 06.23	38 07 57.0	1214 52731 142	1.711	0.0550	7.018	0.185	0.140	0.0437	1.169	1.203
52	09 32 48.77	58 25 30.6	452 51911 487	2.483	0.0323	5.143	0.265	0.196	0.0483	1.084	1.026
53	09 38 13.49	54 28 25.0	556 51991 224	1.865	0.0394	5.764	0.216	0.163	0.0428	1.115	1.126
54	09 51 15.96	36 40 31.1	1596 52998 311	2.951	0.0253	3.701	0.358	0.264	0.0420	1.115	0.878
55	09 51 15.96	36 40 31.1	1595 52999 532	3.094	0.0284	3.691	0.367	0.256	0.0425	1.161	0.864
56	09 54 08.41	54 46 07.0	769 52282 575	2.648	0.0412	6.452	0.221	0.169	0.0475	1.089	0.983
57	09 57 21.27	36 52 44.7	1596 52998 479	2.389	0.0169	3.368	0.195	0.164	0.0371	1.008	0.915
58	10 03 07.78	13 03 26.0	1744 53055 450	3.053	0.0288	4.653	0.287	0.232	0.0679	1.078	1.106
59	10 09 50.24	11 04 39.3	1597 52999 358	2.146	0.0329	5.216	0.251	0.189	0.0385	1.085	0.983
60	10 11 39.16	10 10 42.2	1597 52999 251	2.686	0.0373	6.153	0.263	0.198	0.0507	1.071	1.009
61	10 12 42.97	61 33 02.7	771 52370 490	2.340	0.0520	6.619	0.203	0.141	0.0520	1.170	1.105
62	10 12 57.26	39 28 50.2	1357 53034 202	1.600	0.0563	7.461	0.158	0.126	0.0367	1.154	1.126

Table A1. Continued.

No ^a	RA ^b	DEC ^c	Spectrum ^d number	[O II] λ3727	[O III] λ4363	[O III] λ4959+λ5007	[S II] λ6717	[S II] λ6731	[O II] λ7325	t _{3,O}	t _{2,O}
63	10 21 06.34	36 04 08.7	1957 53415 258	2.484	0.0372	5.072	0.299	0.209	0.0496	1.142	1.040
64	10 28 47.65	39 49 41.5	1428 52998 568	2.808	0.0265	4.567	0.289	0.223	0.0472	1.056	0.951
65	10 29 09.30	39 44 26.0	1430 53002 389	2.460	0.0306	5.115	0.264	0.185	0.0397	1.066	0.932
66	10 33 28.52	07 08 01.7	999 52636 517	2.327	0.0168	3.464	0.216	0.175	0.0361	0.998	0.914
67	10 42 40.51	37 55 02.6	1998 53433 490	2.079	0.0393	5.497	0.216	0.168	0.0521	1.132	1.189
68	10 45 20.41	09 23 49.1	2147 53491 514	1.916	0.0472	6.212	0.208	0.158	0.0511	1.156	1.237
69	10 45 54.47	01 04 05.7	275 51910 445	1.924	0.0447	6.422	0.184	0.137	0.0424	1.122	1.100
70	10 47 23.60	30 21 44.2	1981 53463 438	2.313	0.0350	5.820	0.192	0.145	0.0415	1.068	0.983
71	10 51 08.88	13 19 27.9	1749 53357 026	2.914	0.0388	5.020	0.337	0.241	0.0543	1.164	1.002
72	10 53 28.95	43 30 26.1	1362 53050 466	3.288	0.0148	3.112	0.343	0.255	0.0417	0.993	0.834
73	10 56 39.16	67 10 48.9	490 51929 401	3.263	0.0216	4.736	0.290	0.208	0.0494	0.980	0.904
74	10 59 40.96	08 00 56.8	1003 52641 327	1.883	0.0266	5.874	0.168	0.139	0.0396	0.977	1.071
75	11 09 18.04	49 47 53.7	964 52646 570	2.640	0.0422	5.593	0.267	0.193	0.0485	1.153	0.995
76	11 15 39.03	15 26 12.2	1752 53379 530	2.765	0.0378	5.300	0.303	0.240	0.0653	1.131	1.146
77	11 15 58.16	55 48 06.5	908 52373 027	2.866	0.0438	5.396	0.273	0.192	0.0456	1.184	0.925
78	11 18 48.62	30 36 32.2	1979 53431 240	2.486	0.0397	5.627	0.255	0.198	0.0524	1.127	1.072
79	11 19 59.99	34 38 00.3	2111 53467 232	2.359	0.0437	6.856	0.269	0.166	0.0375	1.089	0.925
80	11 25 46.79	47 00 00.3	1442 53050 396	2.669	0.0197	4.742	0.230	0.164	0.0433	0.952	0.934
81	11 26 40.81	35 20 40.6	2111 53467 018	3.265	0.0218	4.339	0.331	0.247	0.0566	1.008	0.966
82	11 29 14.28	36 44 55.9	2113 53468 430	2.935	0.0206	5.946	0.230	0.168	0.0430	0.905	0.890
83	11 33 10.56	30 57 17.6	1974 53430 200	2.755	0.0286	5.263	0.279	0.204	0.0547	1.033	1.037
84	11 35 30.91	11 17 17.8	1607 53083 205	2.391	0.0402	5.969	0.252	0.186	0.0418	1.109	0.970
85	11 37 06.18	-03 37 37.1	327 52294 042	2.216	0.0449	6.266	0.217	0.158	0.0479	1.133	1.088
86	11 37 07.19	37 48 33.7	2036 53446 598	2.565	0.0285	5.616	0.224	0.155	0.0493	1.012	1.019
87	11 38 09.69	33 58 05.0	2098 53460 503	2.206	0.0307	5.426	0.221	0.154	0.0367	1.047	0.946
88	11 40 47.42	64 47 10.2	597 52059 586	2.411	0.0478	6.410	0.215	0.143	0.0553	1.149	1.126
89	11 43 06.52	68 07 17.7	492 51955 449	2.657	0.0349	5.033	0.301	0.218	0.0532	1.121	1.042
90	11 43 33.10	53 30 00.6	1015 52734 003	2.470	0.0303	5.378	0.234	0.172	0.0416	1.046	0.952
91	11 49 04.74	15 41 01.8	1761 53376 601	3.378	0.0416	5.193	0.300	0.230	0.0583	1.178	0.963
92	11 51 49.13	31 30 14.5	1991 53446 200	3.118	0.0388	4.826	0.323	0.207	0.0488	1.180	0.918
93	11 52 30.06	07 07 03.9	1622 53385 193	2.857	0.0298	4.562	0.321	0.223	0.0500	1.098	0.970
94	11 54 31.91	08 34 37.5	1622 53385 403	2.043	0.0434	5.885	0.202	0.152	0.0453	1.144	1.104
95	11 56 05.17	14 21 31.5	1763 53463 225	2.777	0.0326	4.792	0.272	0.216	0.0639	1.113	1.128
96	12 07 25.64	62 34 57.9	778 52337 498	2.284	0.0208	4.195	0.247	0.196	0.0375	1.004	0.940
97	12 11 19.64	38 23 30.8	2108 53473 077	2.280	0.0222	4.839	0.210	0.158	0.0404	0.981	0.976
98	12 13 49.66	61 25 29.0	779 52342 218	2.646	0.0227	4.784	0.272	0.199	0.0512	0.991	1.023
99	12 20 40.85	33 31 28.0	1999 53503 119	2.684	0.0184	3.764	0.292	0.216	0.0429	1.000	0.927
100	12 24 41.76	14 58 04.6	1767 53436 514	2.282	0.0399	5.865	0.222	0.165	0.0587	1.113	1.209
101	12 25 57.50	39 21 56.9	1986 53475 136	2.325	0.0497	6.578	0.231	0.165	0.0684	1.154	1.323
102	12 27 20.15	51 39 43.3	884 52374 216	2.521	0.0357	5.708	0.256	0.191	0.0417	1.082	0.943
103	12 28 08.06	07 54 43.4	1627 53473 426	2.130	0.0544	7.139	0.188	0.150	0.0529	1.158	1.182
104	12 48 58.09	47 01 37.4	1455 53089 076	2.617	0.0454	5.949	0.258	0.188	0.0503	1.159	1.019
105	12 49 54.84	06 06 10.3	847 52426 522	2.615	0.0404	5.288	0.267	0.190	0.0383	1.159	0.890
106	12 52 14.32	00 51 58.4	292 51609 566	2.537	0.0419	6.432	0.214	0.167	0.0535	1.097	1.072
107	12 53 21.75	50 24 17.8	1279 52736 546	2.044	0.0492	6.817	0.188	0.146	0.0468	1.136	1.125
108	12 53 28.60	58 40 21.9	957 52398 210	2.060	0.0536	7.109	0.189	0.147	0.0494	1.153	1.157
109	12 57 34.42	15 22 29.2	1771 53498 429	2.839	0.0274	4.183	0.345	0.245	0.0662	1.098	1.137
110	13 01 19.26	12 39 59.4	1695 53473 627	2.280	0.0231	4.440	0.212	0.175	0.0424	1.019	1.001
111	13 02 04.39	42 48 12.3	1458 53119 543	3.359	0.0244	3.782	0.357	0.259	0.0504	1.093	0.900
112	13 07 28.69	54 26 49.6	1039 52707 119	2.701	0.0342	6.376	0.196	0.160	0.0518	1.030	1.018
113	13 12 35.15	12 57 43.3	1697 53142 415	2.381	0.0477	6.731	0.206	0.156	0.0489	1.129	1.057
114	13 16 44.77	10 57 32.9	1697 53142 048	1.839	0.0536	7.344	0.178	0.134	0.0456	1.140	1.181
115	13 20 32.02	40 59 01.5	1462 53112 184	2.591	0.0278	4.982	0.195	0.165	0.0547	1.042	1.073
116	13 21 14.47	46 05 04.7	1461 53062 068	2.487	0.0299	5.112	0.196	0.148	0.0431	1.059	0.965
117	13 21 51.93	47 08 35.9	1461 53062 582	2.262	0.0603	6.996	0.224	0.171	0.0540	1.211	1.154
118	13 24 55.03	57 45 10.6	959 52411 137	1.699	0.0644	7.740	0.139	0.109	0.0466	1.194	1.261
119	13 26 38.45	42 14 53.6	1462 53112 608	3.031	0.0163	3.318	0.330	0.240	0.0425	1.002	0.872
120	13 27 38.26	32 09 51.4	2110 53467 409	2.563	0.0165	3.312	0.244	0.190	0.0321	1.006	0.829
121	13 28 44.05	43 55 50.5	1376 53089 637	2.209	0.0336	5.466	0.193	0.150	0.0433	1.075	1.030
122	13 29 23.46	-03 15 02.2	911 52426 253	2.390	0.0266	4.708	0.252	0.183	0.0441	1.047	0.997
123	13 34 44.88	59 44 34.2	960 52425 368	2.899	0.0354	4.383	0.333	0.246	0.0490	1.182	0.953
124	13 34 44.88	59 44 34.2	960 52466 364	3.284	0.0311	4.256	0.324	0.230	0.0529	1.140	0.931
125	13 37 02.29	05 29 11.3	853 52374 540	2.488	0.0305	5.305	0.292	0.209	0.0579	1.053	1.136

Table A1. Continued.

No ^a	RA ^b	DEC ^c	Spectrum ^d number	[O II] λ3727	[O III] λ4363	[O III] λ4959+λ5007	[S II] λ6717	[S II] λ6731	[O II] λ7325	t _{3,O}	t _{2,O}
126	13 37 57.46	12 09 41.6	1700 53502 461	2.447	0.0470	6.096	0.261	0.189	0.0564	1.162	1.129
127	13 40 49.08	38 24 44.2	2005 53472 106	2.293	0.0121	3.324	0.212	0.167	0.0403	0.919	0.972
128	13 41 06.77	60 53 47.5	785 52339 079	3.509	0.0199	4.104	0.298	0.237	0.0555	0.997	0.923
129	13 42 52.05	05 14 15.2	854 52373 373	3.021	0.0189	4.861	0.277	0.215	0.0522	0.935	0.964
130	13 44 27.36	56 01 29.7	1321 52764 624	2.484	0.0449	6.570	0.217	0.174	0.0567	1.115	1.123
131	13 44 27.36	56 01 29.7	1322 52791 470	2.679	0.0420	6.544	0.217	0.178	0.0618	1.091	1.130
132	13 48 06.98	26 24 19.6	2115 53535 414	2.432	0.0665	7.309	0.191	0.144	0.0483	1.235	1.037
133	13 50 43.51	24 34 24.6	2115 53535 215	3.488	0.0142	3.551	0.369	0.272	0.0356	0.942	0.762
134	13 52 20.71	38 48 49.7	2014 53460 525	3.024	0.0344	4.507	0.321	0.225	0.0527	1.158	0.968
135	13 52 48.26	11 14 10.6	1702 53144 234	2.910	0.0254	5.169	0.264	0.189	0.0457	1.001	0.920
136	13 56 24.45	57 45 47.1	1158 52668 120	3.900	0.0321	4.457	0.324	0.256	0.0633	1.135	0.934
137	14 09 34.94	06 10 23.6	1824 53491 063	2.133	0.0452	7.085	0.187	0.137	0.0530	1.089	1.182
138	14 10 07.10	45 08 17.5	1467 53115 579	3.254	0.0282	4.160	0.356	0.267	0.0466	1.112	0.880
139	14 10 22.26	44 14 55.8	1467 53115 032	2.848	0.0357	4.979	0.308	0.208	0.0505	1.134	0.977
140	14 16 43.53	09 00 50.6	1811 53533 347	2.756	0.0329	5.187	0.308	0.233	0.0681	1.087	1.178
141	14 27 09.15	12 58 45.5	1708 53503 512	2.919	0.0271	4.573	0.273	0.206	0.0500	1.063	0.960
142	14 31 04.65	23 00 48.1	2136 53494 265	2.227	0.0286	5.942	0.238	0.185	0.0699	0.996	1.386
143	14 40 57.31	12 20 12.9	1710 53504 632	2.563	0.0302	4.646	0.326	0.228	0.0581	1.096	1.118
144	14 48 25.52	63 10 10.6	609 52339 454	2.481	0.0379	5.709	0.259	0.190	0.0498	1.104	1.043
145	14 48 39.66	54 40 05.0	1163 52669 465	2.423	0.0316	5.633	0.252	0.198	0.0616	1.044	1.200
146	15 09 09.03	45 43 08.8	1050 52721 274	2.130	0.0468	6.701	0.162	0.129	0.0386	1.123	0.988
147	15 10 28.60	34 16 18.4	1385 53108 559	2.882	0.0213	4.718	0.338	0.240	0.0495	0.976	0.961
148	15 12 12.85	47 16 30.7	1050 52721 402	2.271	0.0316	5.197	0.224	0.172	0.0446	1.071	1.031
149	15 16 34.76	30 06 53.6	1650 53174 305	2.573	0.0337	5.435	0.234	0.181	0.0490	1.079	1.014
150	15 28 17.18	39 56 50.4	1293 52765 580	2.168	0.0500	6.913	0.196	0.153	0.0553	1.137	1.202
151	15 28 21.97	36 24 09.4	1401 53144 397	1.993	0.0458	7.154	0.176	0.133	0.0463	1.090	1.135
152	15 30 41.26	31 01 06.5	1388 53119 189	2.076	0.0443	6.578	0.200	0.154	0.0482	1.109	1.134
153	15 36 56.44	31 22 48.0	1388 53119 039	2.914	0.0347	5.404	0.250	0.174	0.0439	1.092	0.902
154	15 37 53.31	58 41 37.7	615 52347 590	2.966	0.0448	5.987	0.268	0.197	0.0581	1.150	1.029
155	15 46 13.86	32 56 32.3	1580 53145 418	2.241	0.0353	5.526	0.242	0.173	0.0483	1.089	1.086
156	15 46 13.86	32 56 32.3	1403 53227 302	2.520	0.0340	5.169	0.228	0.184	0.0579	1.100	1.127
157	15 58 22.20	36 11 43.7	1682 53173 277	2.368	0.0370	6.074	0.226	0.178	0.0532	1.073	1.112
158	15 58 42.48	17 21 37.5	2196 53534 331	2.776	0.0354	5.894	0.224	0.173	0.0492	1.068	0.977
159	16 01 35.95	31 13 53.7	1405 52826 395	3.050	0.0351	5.485	0.197	0.150	0.0426	1.090	0.870
160	16 02 03.58	29 26 14.2	1578 53496 438	2.919	0.0298	5.189	0.291	0.215	0.0533	1.052	0.992
161	16 15 53.92	27 11 43.5	1576 53496 378	2.335	0.0376	5.145	0.262	0.188	0.0449	1.140	1.019
162	16 18 32.65	27 43 52.4	1576 53496 446	1.886	0.0265	6.272	0.181	0.138	0.0395	0.957	1.068
163	16 24 10.10	-00 22 02.5	364 52000 187	1.468	0.0582	7.933	0.127	0.092	0.0359	1.142	1.171
164	16 24 21.38	27 04 08.7	1408 52822 221	2.441	0.0307	5.352	0.243	0.182	0.0442	1.051	0.987
165	16 29 34.81	30 33 29.8	1685 53463 234	2.719	0.0213	4.746	0.297	0.208	0.0428	0.975	0.921
166	16 35 27.94	22 25 18.8	1571 53174 155	2.455	0.0273	5.161	0.260	0.191	0.0428	1.025	0.968
167	16 47 25.17	30 27 29.2	1342 52793 537	2.745	0.0212	4.070	0.263	0.204	0.0460	1.020	0.949
168	16 59 43.89	24 55 50.6	1693 53446 198	2.354	0.0229	4.941	0.324	0.244	0.0448	0.985	1.014
169	17 03 05.08	25 31 47.6	1693 53446 541	3.259	0.0254	3.682	0.318	0.240	0.0412	1.119	0.833
170	17 24 37.52	56 28 37.7	367 51997 561	3.289	0.0281	5.375	0.291	0.208	0.0611	1.021	1.001
171	17 24 37.52	56 28 37.7	357 51813 568	3.575	0.0392	5.573	0.302	0.221	0.0576	1.126	0.931
172	21 04 15.71	-06 05 17.3	637 52174 526	2.482	0.0272	5.242	0.246	0.185	0.0458	1.019	0.997
173	21 15 27.07	-07 59 51.4	639 52146 242	1.757	0.0357	6.265	0.183	0.134	0.0348	1.050	1.036
174	21 39 56.50	00 19 21.7	1108 53227 397	1.874	0.0531	6.857	0.232	0.178	0.0527	1.164	1.282
175	21 46 42.28	00 00 08.9	1030 52914 077	1.924	0.0506	7.041	0.175	0.139	0.0368	1.134	1.016
176	22 15 89.25	01 09 39.0	1034 52525 551	2.651	0.0487	5.654	0.256	0.196	0.0488	1.210	0.996
177	22 15 89.25	01 09 39.0	1034 52813 521	2.369	0.0435	5.544	0.272	0.192	0.0420	1.170	0.977
178	22 15 89.25	01 09 39.0	1476 52964 530	2.576	0.0498	5.631	0.267	0.197	0.0423	1.222	0.940
179	22 51 40.31	12 27 13.3	741 52261 279	2.490	0.0395	5.582	0.238	0.176	0.0422	1.128	0.955
180	23 29 36.55	-01 10 56.9	384 51821 281	2.057	0.0650	7.554	0.196	0.138	0.0433	1.210	1.071
181	23 29 36.55	-01 10 56.9	681 52199 201	1.806	0.0670	7.680	0.191	0.146	0.0422	1.216	1.139

^a The objects are listed in order of right ascension.^b Units of right ascension are hours, minutes, and seconds.^c Units of declination are degrees, arcminutes, and arcseconds.^d The spectrum number is composed of the SDSS plate number, the modified Julian date of the observation, and the number of the fiber on the plate.